FISEVIER

Contents lists available at ScienceDirect

# Journal of Electroanalytical Chemistry

journal homepage: www.elsevier.com/locate/jelechem



# Corrosion inhibition of mild steel in acidic medium by simple azole-based aromatic compounds



Eugene B. Caldona <sup>a,b</sup>, Min Zhang <sup>a</sup>, Guangchao Liang <sup>a</sup>, T. Keith Hollis <sup>a</sup>, Charles Edwin Webster <sup>a</sup>, Dennis W. Smith Jr <sup>a,b</sup>, David O. Wipf <sup>a,b,\*</sup>

- <sup>a</sup> Department of Chemistry, Mississippi State University, Mississippi State, MS 39762, United States
- b Marvin B. Dow Advanced Composites Institute, Mississippi State University, Mississippi State, MS 39762, United States

# ARTICLE INFO

Article history:
Received 12 June 2020
Received in revised form 11 November 2020
Accepted 11 November 2020
Available online 17 November 2020

Keywords:
Azole derivative
Mild steel
Corrosion inhibitor
EIS
Potentiodynamic polarization

#### ABSTRACT

Many organic corrosion inhibitors are complex and may include complicated chemical structures, mixture of different species, or require numerous and tedious preparation steps. In this study, we demonstrate inhibition by triazole- and imidazole-based compounds, which are synthesized in a one-step method and possess austere chemical structures. The inhibition effect was studied on the corrosion of mild steel in 1.0 M HCl solution at 40 °C by electrochemical impedance spectroscopy (EIS), potentiodynamic polarization, and weight loss. Results from electrochemical measurements showed that the aromatic compounds were effective in inhibiting corrosion in acidic medium, such that the inhibition efficiency increased with increasing inhibitor concentration. The triazole-based compound had the best inhibitive performance (efficiency >90%), followed by the imidazole-based (~85%), at a concentration of 850  $\mu$ M. These results were supported by analyses obtained from scanning electron and atomic force microscopy, which showed improved mild steel topology and decrease in surface roughness by up to a factor of five, and x-ray diffraction, which revealed the extent of oxide layer formation. In addition, the adsorption of a protective inhibitor layer on the metal surface was confirmed by Raman spectroscopy, while the underlying mode and mechanism were postulated based on a Langmuir adsorption isotherm and computational studies, which showed good correlation between the inhibitive ability and the electron donating and accepting capability of the compounds.

# 1. Introduction

Mild steel (MS) is one of the most widely used engineering materials owing to its outstanding mechanical properties, low cost, and ready availability [1,2]. Its high vulnerability to corrosion attack, however, limits some of its applications [2,3]. For instance, the use of acidic solutions during acid pickling, acid descaling, and other industrial acidification processes induces hydrogen embrittlement, leading to structural damage and severe corrosion [2–4]. Hence, protecting MS from such corrosive environments is necessary. Many polymeric composites and fluorinated materials have been used as corrosion protection coatings [5–8]. However, the use of corrosion inhibitors has proven to be one of the most practical and effective means of combating corrosion in an acidic environment mainly due to their cost-effectiveness and ease of application [9].

Corrosion inhibitors are chemical compounds, which when added in very small quantities to an aggressive medium effectively slow down the corrosion rate by acting or selectively retarding the cathodic and/or anodic reactions [9]. Their inhibiting property lies in their ability to adsorb and form a protection barrier across the metal surface

[9–11]. Inorganic compounds [12] containing phosphates, molybdates, nitrates, and chromates have long been known as efficient corrosion inhibitors that adsorb on the metal surface and form a passivation layer of mono- or polyatomic oxide film-effectively retarding the oxidation of metals in several aggressive media. However, many of these compounds, including their derivatives, are toxic and pose serious environmental and health risks [13]. Alternatively, many organic inhibitors are considered nontoxic, environment-friendly materials. They have been shown to minimize corrosion by adsorbing onto the metal surface and forming a thin protective layer that blocks active corrosion sites [9-11]. This reduction, however, is strongly dependent on the molecular structure of the organic inhibitor, particularly its planarity and the overall molecular spatial orientation [14,15].  $\pi$  electrons, polar groups, and heteroatoms with electron lone pairs also play a vital role as they can serve as reactive sites of the inhibitor molecules during the course of adsorption and interaction with the metal surface [14,15]. Hence, organic compounds that contain combinations of S, O, P, N, aromatic rings, and multiple bonds have been shown to function effectively as corrosion inhibitors in acidic solutions [9-11].

<sup>\*</sup> Corresponding author at: Department of Chemistry, Mississippi State University, Mississippi State, MS 39762, United States. E-mail address: DWipf@chemistry.msstate.edu. (D.O. Wipf).

Among the widely known commercially available organic inhibitors are alkenylphenones, acetylenic alcohol derivatives, quaternary ammonium complexes, and aromatic aldehydes [16,17]. Extended use of these compounds, however, may be harmful to the environment and cause adverse health effects [17]. Many well-known drug-based compounds have become ideal substitutes for commercial toxic corrosion inhibitors in acidic solutions for MS [10,18–22]. For example, 500 µM clozapine in 1.0 M HCl solution inhibited MS corrosion at 92.8% efficiency [18]. Ketosulfone drug at 200 ppm in HCl solution yielded an efficiency of 83.6% [19]. 400 ppm cefalexin [20] and 500 ppm streptomycin [21] in individual acidic solutions reached efficiencies of 94% and 84.8%, respectively. 300 ppm Modazar was also proven effective and reached 86.9% inhibition efficiency in HCl solution [22]. Their main downside, however, is their costly synthetic preparation. Also, due to their structural complexity and possible interference of other trace pharmaceutical components, their exact corrosion inhibition mechanism has yet to be investigated [10]. Natural organic products such as plant, leaf, and fruit peel extracts have also been developed as green corrosion inhibitors because of their ecofriendliness and nontoxicity [11,23-26]. 200 ppm Ginkgo leaf extract in HCl solution was shown to inhibit corrosion at 90% efficiency [23]. Extracts of Ligularia fischeri [24] and Tragia plukenetii [25], both at 500 ppm, yielded efficiencies of 66% and 75%, respectively, in acidic solutions.  $2 \text{ g L}^{-1}$  Ircinia strobilina extract in acidic medium was also shown to be efficient at 83.8% [26]. Due to the presence of a wide variety of components in the extract, their major drawback lies in the tediousness of their separation processes and the lack of their complete phytochemical investigation, in which the identification of the active ingredients and understanding of the inhibition mechanism remain an issue [11]. These shortcomings explain why research and advancement on corrosion inhibitors is dynamically explored from a wide range of perspectives, all of which are concerned with developing, not only nontoxic and environmentally friendly inhibitors, but also those that require fewer synthetic or preparation steps, have fewer components, and have less complex chemical structures. Further, these inhibitors must be inexpensive and effective at concentrations in the  $\mu M$  or ppm level, or lower.

Azole compounds form an important class of corrosion inhibitors that have always drawn a great deal of interest among researchers [27-32]. Azoles are five-membered heterocyclic nitrogen-containing compounds and their derivatives are among the most promising organic corrosion inhibitors [27,33]. The most popularly reported having useful inhibitive properties are derivatives of pyrazoles, benzimidazoles, benzotriazoles, tetrazoles, oxazoles, and thiazoles [27,29,30,32,34]. Ouici et al. [29] reported the inhibition of 5-amino-1,3,4-thiadiazole-2-thiol on MS, with 91.5% efficiency at 2 mM concentration in 1.0 M HCl solution. Dutta et al. [30] studied the effect of phenyl-substituted benzimidazole derivatives on corrosion inhibition of MS and efficiencies as high as 93.7% were achieved in 1.0 M HCl solution. Haque and co-workers [31] synthesized 2-amino-3-((4-((S)-2-amino-2carboxyethyl)-1H-imidazol-2-yl)thio)propionic acid and its efficiency as a corrosion inhibitor for MS at 0.365 mM in HCl solution was reported at 94.1%. Ansari et al. [32] also showed that the presence of 150 mg  $L^{-1}$  pyridyl substituted triazoles in HCl solution inhibits MS corrosion at 95% efficiency. A review by Faisal et al. [35], which focused on the general properties and inhibition efficiencies of different triazole derivatives for MS corrosion, provides useful information on inhibitor underlying mechanisms and suitability in various acidic environments.

Although numerous reports on azole-based compounds as corrosion inhibitors are available, only a few have considered the difficulty of their synthesis and level of toxicity when used at high concentrations [27,28,30]. In this study, we report the use of one-step-synthesized azole-based compounds–1,2-bis(imidazoyl)benzene, 1,3-bis(imidazoyl)benzene, and 1,3-bis-1,2,4-triazoylbenzene (Fig. 1: 12i, 13i, and 13t, respectively)—as less complex, inexpensive, and environmentally friendly corrosion inhibiting agents for MS in acidic medium. In general, unmodified imidazole and triazole are almost never used as corrosion inhibitors because of their low surface activity and low heteroatom reactivity [33,36]. Herein, we show that a benzene ring with at least two substituted imidazole or triazole groups can effectively adsorb on MS surface and display enhanced corrosion inhibition even at very low concentrations. To the best of our

Fig. 1. Structures of the azole inhibitors in this study.

knowledge, these azole-based compounds have not been reported as corrosion inhibitors for MS in an acidic solution. The corrosion inhibition is examined in HCl as it is among the most extensively used acids in many acidification processes [3,9]. The inhibition properties are evaluated mainly by potentiodynamic polarization, electrochemical impedance spectroscopy (EIS), and weight loss, supported by surface imaging, spectroscopic analyses, adsorption study, and quantum chemical computations.

#### 2. Experimental

#### 2.1. Materials

The substrates used were  $25 \times 38 \times 1$  mm MS sheets (ASTM A366/1008 cold-rolled, OnlineMetals) with nominal composition (wt%) of 0.04 S, 0.035 P, 0.08 C, 0.2 Cu, 0.6 Mn, and Fe making up the remainder. A Metaserv Grinder-Polisher (Buehler), with 240, 400, and 800 SiC paper, was used to grind the MS substrates prior to use. HPLC Plus Grade acetone ( $\geq 99.9\%$ , Sigma-Aldrich) was used to wash and degrease the ground substrates via sonication for 10–15 min, followed by air drying.

12i, 13i, 13t and monosubstituted analogues 1,2,4-triazoylbenzene (1t) and imidazoylbenzene (1i) were prepared according to previous reports [37–39]. Synthesis details are described in the Supplementary Information. Commercially available 1,2,4-triazole (t) and imidazole (i) (99%, Alfa-Aesar) were also studied for comparison. The inhibited test solutions were made by preparing 50, 250, 550, and 850  $\mu M$  inhibitor in 1.0 M HCl solution. 12.1 N HCl (Fisher Scientific) was diluted with 18.0 M $\Omega$  cm resistivity deionized water to prepare 1.0 M HCl solution.

# 2.2. Characterization and instrumentation

All electrochemical experiments were executed in a conventional threeelectrode cell using a saturated calomel electrode (SCE) as reference, a graphite rod as counter, and a MS substrate as working electrodes. The geometric surface area of the MS and counter electrodes in solution was 14 and 25 cm<sup>2</sup>, respectively. The electrolyte solution was 1.0 M HCl, held at 40 °C and stirred at 350 rpm with a magnetic stir bar. Potentiodynamic polarization and electrochemical impedance spectroscopy (EIS) were carried out using a Solartron Analytical 1470E potentiostat/galvanostat equipped with a Solartron SI 1250 frequency analyzer. Immersion in solution with and without the presence of an inhibitor, was done for 30 min to allow the substrates to freely corrode and ensure a steady-state open-circuit potential (OCP). EIS measurements were then performed using a 10 mV AC amplitude about the OCP from 100 mHz to 60 kHz. The resulting impedance data were fitted to equivalent electrical circuits (EEC) using ZView (Scribner Associates). Potentiodynamic polarization curves were also obtained by scanning the potential from -0.25 to +0.25 V versus SCE about the OCP at a rate of 1.0 mV s<sup>-1</sup>. Corrosion current densities  $(I_{corr})$ and potentials  $(E_{corr})$  were obtained using CView (Scribner Associates) from extrapolation of the linear Tafel plots of the cathodic and anodic curves. Measurements at each concentration were repeated three or more times.

Weight loss measurements of the MS substrates were done in an unstirred 1.0~M HCl solution at  $40~^{\circ}$ C in the absence and presence of a corrosion inhibitor at  $850~\mu$ M. After immersion for 12~h, the substrates were carefully rinsed with deionized water and vacuum-dried to constant weight. After following the same experimental conditions for the electrochemical measurements, but with a 4-h extended immersion time, scanning electron microscopy (SEM) and elemental analysis were performed with a JEOL 6500F Field Emission SEM equipped with an X-max 80 energy-dispersive x-ray (EDX) spectroscopy detector (Oxford Instruments) at 20~kV. Three-dimensional atomic force microscopy (AFM) images were acquired from a Bruker Dimension Icon atomic force microscope. A Rigaku SmartLab high resolution x-ray diffractometer, operated at 40~kV and 44~mA, was used to obtain x-ray diffraction (XRD) patterns from  $3~^{\circ}$  to  $90~^{\circ}$  at a rate of  $1~^{\circ}$  per min. Raman spectra were collected after a 12-h immersion in an unstirred test solution using a Horiba LabRam HR800 confocal Raman microscope with a 632~nm laser excitation.

The adsorption isotherms describing the interaction of the inhibitors with the MS surface were obtained using the surface coverage values  $(\theta)$ , which were calculated using the polarization resistance  $(R_n)$  obtained from the EIS fitting at different inhibitor concentrations. The Gaussian 16 (G16 version A03) [40] electronic structure package was used to perform density functional theory (DFT) computations on the neutral and protonated forms of the inhibitors. Gas-phase geometry optimizations and frequency calculations were performed using the B3LYP [41-44] functional with the 6-31G(d ') [45,46] basis set for all atoms. In Gaussian software, the 6-31G(d ') basis set has the exponent of d polarization functions for C, N, O taken from the 6-311G(d) basis sets, instead of the original arbitrarily assigned exponent of 0.8 used in the 6-31G(d) basis sets. For H, the 6-31G(d'') keyword in Gaussian software utilizes the 6-31G(d) basis sets. The optimized structures and the frontier molecular orbitals (FMO) were modeled, while the energies of the lowest unoccupied molecular orbital ( $E_{\text{LUMO}}$ ) and the highest occupied molecular orbital (E<sub>HOMO</sub>) were extracted from the output.

# 3. Results and discussion

#### 3.1. Potentiodynamic polarization

Fig. 2a displays the time-dependent OCP plots for 30 min of immersion of the uninhibited and inhibited MS samples in 1.0 M HCl solution at 40  $^{\circ}$ C.

The OCP shifted positive with time until near constant values (summarized in Table 1) are attained. The time taken by the inhibited samples to reach near stable OCP varied from 600 to 1500 s. The OCP shift to positive direction with increasing inhibitor concentration is a general indication of formation of a more stable and protective inhibitor layer on MS surface [26]. 13t at 850 µM concentration achieved the highest OCP value, nearly 40 mV more positive than the uninhibited system, followed by 13i and 12i.

Potentiodynamic polarization was performed 30 min after a steady state OCP was reached. This immersion period was chosen to provide insight on the quickest possible time for the inhibitors to take effect. Such inhibitor capability is important for practical applications in acid pickling processes, which have a typical 30-min duration in 1.0 M HCl [47]. A scan rate of 1.0 mV s<sup>-1</sup>, although more rapid than ideal, was chosen to minimize the polarization time and avoid compromising the integrity of the inhibitor film while still acquiring valid data [23,26,31,32]. Thus, these curves and the resulting data points are used to compare the behavior of the inhibitor materials. The resulting Tafel curves are shown in Fig. 2b, while the extracted electrochemical parameters  $I_{corr}$ ,  $E_{corr}$ , and the anodic  $(\beta_a)$  and cathodic  $(\beta_c)$  slopes are given in Table 1. The inhibition efficiency (IE% $_p$ ) was estimated using the  $I_{corr}$  values:

$$IE\%_{\rho} = \frac{I_{corr,u} - I_{corr,i}}{I_{corr,u}} \times 100\%$$
 (1)

where  $I_{corr,u}$  and  $I_{corr,i}$  are the corrosion current density of the MS in the uninhibited (blank HCl solution with no inhibitor) and inhibited (HCl with an inhibitor) solutions, respectively.

Analysis of the Tafel plots in Fig. 2b reveals that the azole-based compounds are able to reduce both the anodic and cathodic current densities and the effect becomes more prominent at higher concentrations, which shows that the compounds are effective in inhibiting both the anodic dissolution of metallic Fe and cathodic evolution of hydrogen. The increase in corrosion inhibition with the inhibitor concentration (Table 1) suggests that the azole compounds worked by adsorption on the MS surface to form a thin layer of protective film [27,33,36]. In contrast to the blank HCl solution that yielded an  $I_{corr}$  value of 3433.4  $\pm$  10.0  $\mu$ A cm<sup>-2</sup>, much lower  $I_{corr}$  values of 618.0  $\pm$  15.4, 582.3  $\pm$  16.2, and 245.4  $\pm$  7.6  $\mu$ A cm<sup>-2</sup> were obtained in the presence of 850  $\mu$ M of 12i, 13i, and

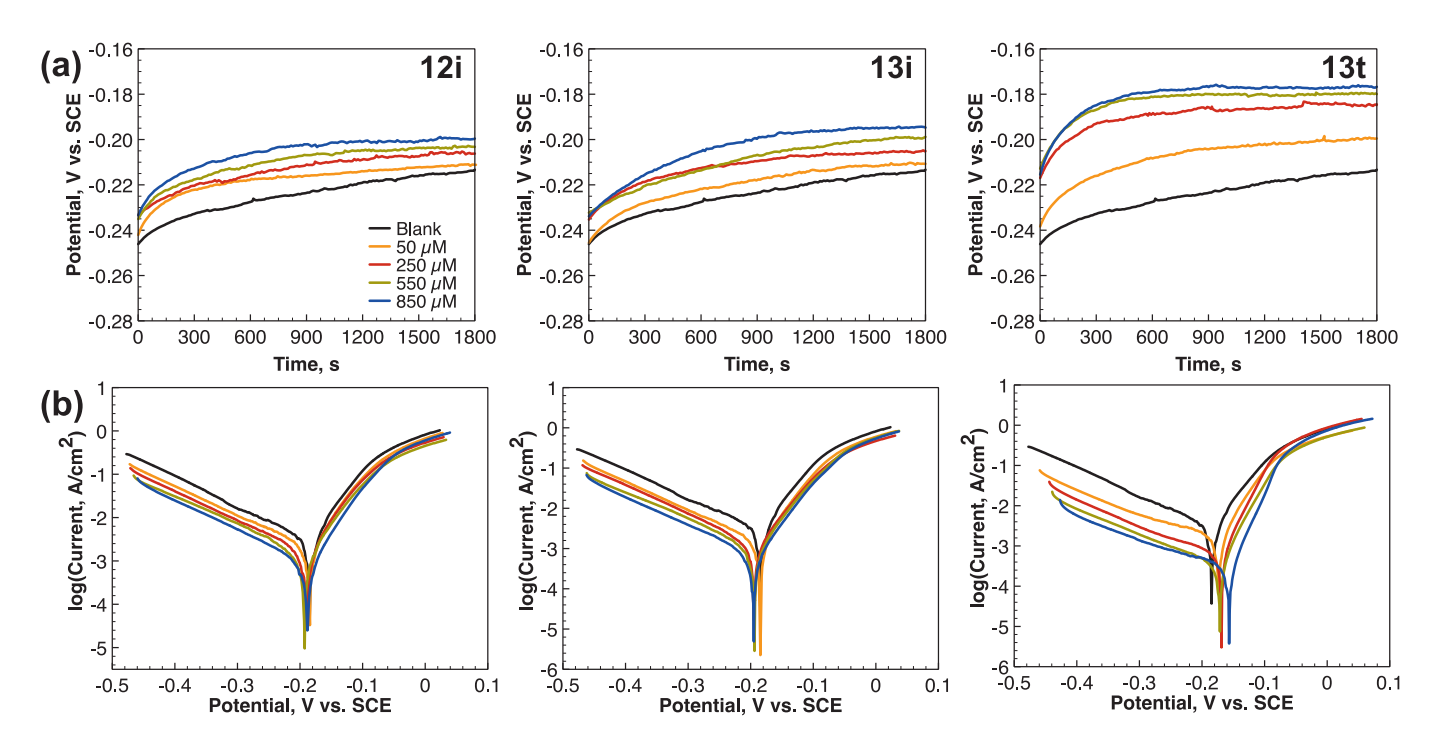


Fig. 2. (a) OCP and (b) Tafel curves for MS in 1.0 M HCl solution at 40 °C in the absence and presence of 12i, 13i, and 13t at different concentrations.

**Table 1**Tafel parameters and OCP values for MS in uninhibited and inhibited 1.0 M HCl solution at 40 °C.

	$eta_a$	$-\beta_c$	$I_{corr}$	$-E_{corr}$	OCP	IE% <sub>ρ</sub>
	mV decade <sup>-1</sup>	mV decade <sup>-1</sup>	μA cm <sup>-2</sup>	mV vs. SCE	mV vs. SCE	
Blank	57.6 ± 1.2	148.4 ± 2.9	3433.4 ± 10.0	187.7 ± 1.8	$-212.6 \pm 7.3$	_
13t						
50 μM	$32.7 \pm 0.9$	$152.9 \pm 1.5$	$808.3 \pm 5.9$	$173.4 \pm 1.0$	$-196.3 \pm 5.8$	~76.5
250 μΜ	$31.7 \pm 0.5$	$162.0 \pm 1.6$	$492.2 \pm 9.6$	$169.5 \pm 0.7$	$-184.5 \pm 0.5$	~85.7
550 μM	$38.7 \pm 1.3$	$163.4 \pm 1.1$	$349.4 \pm 8.9$	$176.6 \pm 1.6$	$-181.3 \pm 1.7$	~89.8
850 μΜ	$35.5 \pm 1.6$	$173.1 \pm 2.2$	$245.4 \pm 7.6$	$168.9 \pm 3.0$	$-175.5 \pm 4.6$	~92.9
13i						
50 μM	$42.5 \pm 2.0$	$111.3 \pm 3.7$	$1085.3 \pm 23.3$	$183.4 \pm 1.2$	$-208.6 \pm 3.6$	~68.4
250 μΜ	$47.7 \pm 1.2$	$110.0 \pm 2.3$	$908.3 \pm 21.7$	$191.6 \pm 0.8$	$-202.8 \pm 1.2$	~73.5
550 μM	$49.5 \pm 1.8$	$106.2 \pm 4.2$	$713.2 \pm 24.3$	$194.2 \pm 1.4$	$-199.0 \pm 5.2$	~79.2
850 μΜ	$50.7 \pm 1.7$	$119.9 \pm 1.3$	$582.3 \pm 16.2$	194.7 ± 1.4	$-195.9 \pm 2.6$	~83.0
12i						
50 μM	$40.2 \pm 1.4$	$110.7 \pm 0.9$	$1281.5 \pm 28.8$	$176.1 \pm 2.4$	$-209.4 \pm 2.4$	~62.7
250 μΜ	$35.1 \pm 2.6$	$104.4 \pm 4.2$	$975.6 \pm 14.6$	$184.2 \pm 1.7$	$-204.5 \pm 1.7$	~71.6
550 μM	$39.9 \pm 2.0$	$104.6 \pm 4.0$	$782.8 \pm 13.5$	$188.1 \pm 0.9$	$-200.0 \pm 2.1$	~77.2
850 μΜ	$39.0 \pm 0.8$	$116.3 \pm 3.2$	$618.0 \pm 15.4$	$182.2 \pm 0.7$	$-198.4 \pm 1.1$	~82.0

13t, respectively. The shape of the anodic polarization curves for 12i and 13i in Fig. 2b is similar to that acquired in the blank solution and the lines nearly run parallel to each other. This comparison can also be evidenced by their  $\beta_a$  values, which are close to each other. Therefore, adsorbed 12i and 13i molecules do not appear to modify the Fe oxidation mechanism, but are able to block active corrosion sites due to their low  $I_{corr}$  values [23,32]. However, a separate investigation of the effect of temperature will be needed to verify this presumption. It is noteworthy that the cathodic branches of 13t also give rise to almost parallel lines. This observation implies that the presence of 13t does not change the hydrogen evolution mechanism and the H<sup>+</sup> ion reduction on the MS surface follows a charge transfer mechanism [32,33]. The anodic polarization curves for 13t implied good inhibition effect between  $E_{corr}$  and -80 mV due to the formation of an adsorbed inhibitor film. Potentials higher than -80 mV show that the anodic curves changed course and coincided with that of the blank solution [28]. This effect may have been caused by a slight dissolution of Fe, which led to the desorption of the adsorbed 13t molecules from the metal surface. At this stage, the desorption potential, the inhibitor desorption rate is higher than its adsorption rate [34].

Relative to the  $E_{corr}$  of the blank solution, no significant shift in the  $E_{corr}$  of the inhibitors was observed in Table 1. Note that  $E_{corr}$ , in general, is not equal to OCP as the former is measured through polarization technique, which introduces small current disturbances, while the latter is measured in the absence of polarization at zero net current. For all concentrations, the shift in the  $E_{corr}$  was smaller than  $\pm$  85 mV, indicating that the 12i, 13i, and 13 t inhibitors can be classified as mixed-type [29-32], which simultaneously reduce the rate of both cathodic and anodic reactions. The larger positive shift in the Ecorr values of 13 t indicates its slight anodic inhibition character or smaller metal dissolution tendency [30,48]. Non-logarithmic currentpotential curves are shown in Fig. S2 to better illuminate the onset potential for hydrogen evolution reaction (HER) in all solutions. Compared to an onset potential of -203 mV for the blank solution, more negative onset HER potentials were exhibited by the inhibited solutions. In particular, onset potentials of -296, -304, and 380 mV for  $850~\mu\text{M}$  of 12i, 13i, and 13t, respectively, were observed. These results indicate that the rate of reduction of H<sup>+</sup> ions to H<sub>2</sub> gas is minimized [4]. In organic-inhibitor-containing acid solutions, the first step involves the exchange of the adsorbed water molecules on the metal by the inhibitor. In the succeeding steps, the N atoms and the  $\pi$  electrons of the azole and benzene rings, respectively, facilitate the interaction of Fe<sup>2+</sup>, formed during the Fe dissolution, with the adsorbed 13t molecules, generating the Fe(II)-13t complexes that adsorb on the metal surface, and thus, decrease the dissolution rate of MS in HCl solution [32,33].

The symmetry of the cathodic and anodic curves in terms of their energy barrier can be explained by considering the Tafel slopes,  $\beta_c$  and  $\beta_a$ . The larger their values, the better the inhibition properties [30,32]. From Table 1, it can be seen that the values of  $\beta_c$  were higher in the presence of **13**t inhibitor. This

observation implies that **13t** influences the reaction kinetics of the hydrogen evolution by increasing the energy barrier for  $H^+$  discharge, which results in a smaller accessible surface area for  $H^+$  and leads to reduced  $H_2$  gas evolution. This phenomenon decreases the rate of hydrogen evolution, while the actual mechanism of the reaction is unchanged [30,32]. Thus, **13t**, with the highest  $IE\%_\rho$  of  $\sim$ 92.9% at a concentration of 850  $\mu$ M, showed better corrosion inhibition than **12i** and **13i**. The OCP and Tafel plots for **1t**, **1i**, **t**, and **i**, and their extracted electrochemical parameters at a concentration of 850  $\mu$ M in 1.0 M HCl solution, were also obtained and are shown in **Fig. S3** and **Table S1**, respectively, in the Supplementary Information for comparison purposes. It can be seen that these inhibitors displayed lower  $IE\%_\rho$  than any of the **12i**, **13i**, and **13t** inhibitors due to either deficiency in N atoms or lack of a benzene ring, which helps promote stability and electron delocalization within the molecule [30].

# 3.2. EIS study

Impedance measurements were also used in electrochemical investigation of the corrosion inhibition of the azole-based compounds. EIS data were acquired over the frequency range of 100 mHz to 60 kHz at an excitation signal of 10 mV. The Nyquist diagram plots the real impedance Z' versus the imaginary Z''. The Bode plots show the impedance modulus |Z| and phase angle  $\theta$  on separate ordinates versus the frequency f in logarithmic scale along the abscissa. The Nyquist plots for MS in the absence and presence of f 12i, f 13i, and f 13t at different concentrations are shown in Fig. 3. It can be seen that the changes in impedance response of MS were more pronounced with the addition of increasing concentrations of the inhibitors. This observation is evidenced by the growing diameter of the semicircles, which show a capacitive-resistive behavior with a charge transfer resistance. These semicircles were slightly depressed due to the nonuniformity of the MS surface and adsorptive behavior of the inhibitors f 149].

The EIS parameters presented in Table 2 were extracted by fitting and modeling the acquired impedance spectra into an equivalent electrical circuit (EEC) with one time constant. Also shown in Fig. 3 is the simplified Randles circuit model with a solution resistance ( $R_s$ ) in series with a parallel combination of constant phase element (CPE) and polarization resistance ( $R_p$ ), where  $R_p$  is the sum of the resistances due to charge transfer ( $R_{ct}$ ) and film ( $R_t$ ) formation by the inhibitor on the MS surface [49], that is:

$$R_p = R_{ct} + R_f \tag{2}$$

The CPE describes the non-ideal capacitive behavior of MS in the acidic solution and the adsorbed ions in the electrical double layer [49]. It is characterized by an impedance represented as:

$$Z_{\text{CPE}} = Y_0^{-1} (j\omega)^{-n} \tag{3}$$

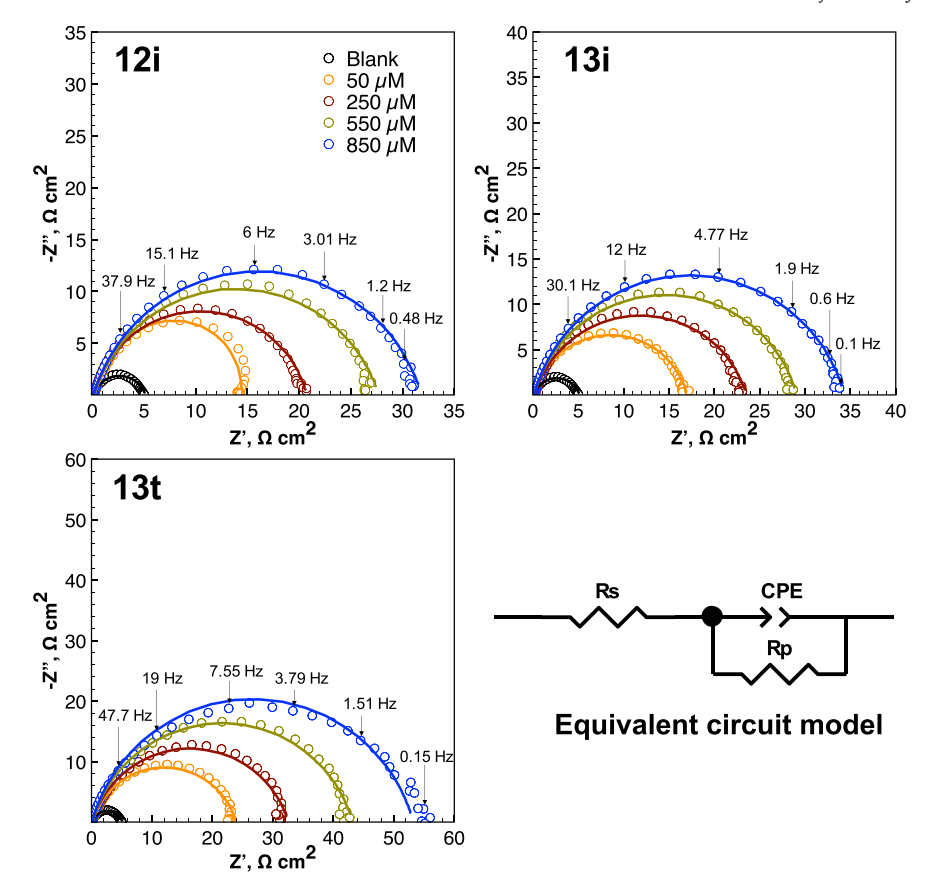


Fig. 3. Nyquist plots and the corresponding equivalent circuit model for MS in 1.0 M HCl solution at 40 °C in the absence and presence of 12i, 13i, and 13t at different concentrations. Fitted data are shown by solid lines.

where  $Y_0$  is the CPE constant,  $j^2 = -1$ ,  $\omega = 2\pi f$  (angular frequency), and n, ranging from 0 to 1, determines the phase shift and accounts for non-ideal capacitive response [50]. The double layer capacitance ( $C_{dl}$ ) is given by the Hsu and Mansfeld [50] equation as:

while the relaxation time constant  $(\tau)$ , which measures the time taken for a charge-transfer process to attain equilibrium after an applied perturbation [49], is represented by:

$$\tau = R_{\rm p}C_{\rm dl} \tag{5}$$

$$C_{\rm dl} = \left(Y_{\rm o}R_{\rm p}^{1-n}\right)^{\frac{1}{n}}$$

 Table 2

 EIS parameters extracted from data fitting for uninhibited and inhibited MS in 1.0 M HCl solution at 40  $^{\circ}$ C.

	$R_p$	$Y_o \times 10^4$		$C_{dl}$	τ		
	$\Omega$ cm <sup>2</sup>	$\Omega^{-1}$ cm <sup>-2</sup> s <sup>n</sup>	n	μF cm <sup>-2</sup>	ms	$\chi^2$	IE%z
Blank	4.7 ± 0.1	30.7 ± 3.0	0.810 ± 0.005	1138.2	5.4	0.005	-
13t							
50 μM	$23.8 \pm 0.2$	$16.5 \pm 0.3$	$0.828 \pm 0.002$	844.8	20.1	0.003	~79.9
250 μΜ	$32.5 \pm 0.3$	$15.3 \pm 0.3$	$0.819 \pm 0.003$	788.3	25.6	0.004	~85.3
550 μM	$43.1 \pm 0.3$	$11.4 \pm 0.2$	$0.827 \pm 0.002$	604.2	26.0	0.003	~88.9
850 μΜ	$53.2 \pm 0.5$	$8.8 \pm 0.2$	$0.832 \pm 0.003$	471.4	25.1	0.004	~91.0
13i							
50 μM	$16.9 \pm 0.1$	$18.4 \pm 0.3$	$0.846 \pm 0.002$	979.1	16.6	0.003	~71.8
250 μΜ	$23.4 \pm 0.2$	$17.0 \pm 0.4$	$0.819 \pm 0.003$	836.4	19.6	0.004	~79.6
550 μM	$29.0 \pm 0.2$	$15.3 \pm 0.3$	$0.831 \pm 0.002$	813.3	23.6	0.003	~83.5
850 μΜ	$34.2 \pm 0.2$	$13.9 \pm 0.2$	$0.835 \pm 0.002$	763.1	26.1	0.001	~86.0
12i							
50 μM	$15.3 \pm 0.3$	$19.8 \pm 0.9$	$0.864 \pm 0.007$	1141.1	17.5	0.010	~68.8
250 μΜ	$20.6 \pm 0.1$	$19.7 \pm 0.4$	$0.847 \pm 0.002$	1105.3	22.8	0.003	~76.8
550 μM	$27.6 \pm 0.2$	$17.9 \pm 0.3$	$0.825 \pm 0.002$	945.2	26.1	0.003	~82.7
850 μΜ	$31.7 \pm 0.2$	$17.3 \pm 0.3$	$0.821 \pm 0.002$	917.8	29.1	0.002	~84.9

The inhibition efficiency based on impedance measurements ( $\text{IE}\%_{\text{Z}}$ ) is expressed by:

$$IE\%_{Z} = \frac{R_{p,i} - R_{p,u}}{R_{p,i}} \times 100\%$$
 (6)

where  $R_{p,u}$  and  $R_{p,i}$  refer to the polarization resistance of MS in the uninhibited and inhibited acidic solutions, respectively.

Satisfactory fits to the EEC model was obtained for all impedance spectra, as indicated by the low chi-squared ( $\chi^2$ ) values in Table 2. It can be seen that the  $R_p$  was higher in the inhibited solutions than in the blank solution and the values increased with increasing inhibitor concentration. 13t had the highest  $R_p$  of 53.2  $\pm$  0.5  $\Omega$  cm<sup>2</sup> at 850  $\mu$ M, which was tenfold that of the blank solution. 13t was followed by 13i and 12i with  $R_p$  values of  $34.2 \pm 0.2$  and  $31.7 \pm 0.2 \Omega$  cm<sup>2</sup> at 850  $\mu$ M, respectively. This result suggests that the azole-based inhibitors adsorbed on the MS surface and formed a protective insulating layer that increased the  $R_{ct}$  at the metalsolution interface, thus, resulting in a slower corroding system [33,36]. Likewise, a corresponding decrease in the  $C_{dl}$  values was observed in the inhibited solutions. From a  $C_{dl}$  of 1138.2  $\mu$ F cm<sup>-2</sup> for the blank solution, the values were reduced to 917.8, 763.1, and 471.4  $\mu$ F cm<sup>-2</sup> for 850  $\mu$ M of 12i, 13i, and 13t, respectively, representing a decrease in the local dielectric constant or an increase in inhibitor film thickness on the metal surface [51]. The double layer at the metal-solution interface can be viewed as an electrical capacitor. Its electrical capacity can be decreased when inhibitor molecules (with low dielectric constants) adsorb on the metal surface and displace adsorbed water molecules and other ionic species (with higher dielectric constants) [51]. As a result, reduced  $C_{dl}$  values imply the presence of an inhibitor film on the metal surface [50,51]. The  $\tau$  values in the inhibited solutions were also smaller, which means that the inhibitor discharge velocity at the interface during adsorption was faster [49]. Compared to those of 13i and 12i, 13t had a smaller  $\tau$  of 25.1 ms at 850  $\mu$ M. The slight increase in the values of n was also noticeable in the inhibited solutions, suggesting some improvement in metal surface homogeneities and smoothness [50], due to the adsorption of the inhibitors.

The Bode magnitude and phase  $(\theta)$  plots (Fig. 4) illustrate that the high frequency region, where the values of  $\log |Z|$  and  $\theta$  fall to zero, describes the resistive behavior of MS due to  $R_s$  [49]. In the low frequency region, where  $\theta$  approaches zero,  $|Z| \approx R_p$ , and the impedance becomes independent of f. The non-ideal capacitive behavior can be explained by the medium frequency region [49,50], where  $\log f$  and  $\log |Z|$  develop a linear relationship, with slope of nearly -1 and  $\theta < 90^\circ$ . Again, such non-ideality is manifested by the flattened semicircles in the Nyquist plots [50], where n < 1. The single maximum peak shown by the Bode  $\theta$  plots (Fig. 4) confirms that the one-time-constant EEC model used to fit the EIS data was appropriate. It also indicates that the uninhibited and inhibited systems involved one relaxation, charge-transfer process at the metal-solution interface and the

inhibitive effect of the azole-based compounds was mainly polarization resistance controlled [33,36]. In the inhibited solutions, the higher  $\theta_{max}$ peaks can be correlated to slower rates of metal dissolution [29,32]. The broadening of the maximum peaks with increasing inhibitor concentration reflects the degree of formation of a protective inhibitor layer [29,31,32], with 13t representing the broadest and highest  $\theta_{max}$  peak at 850 µM. The |Z| at 0.1 Hz in the Bode magnitude plots can also be used to evaluate the protection performance and integrity of the inhibitor films [49]. The increasing  $|Z|_{0.1~\mathrm{Hz}}$  values with inhibitor concentration account for the increasing strength of the inhibitive action, with 13 t exhibiting higher |Z| $_{0.1~\mathrm{Hz}}$  than those for 13i and 12i. The inhibitive performance in terms of IE%<sub>Z</sub> in Table 2 follows the order of 13t > 13i > 12i and a good correlation with the IE%, was obtained. In industrial applications, an effect greater than 87% is required for acid pickling [9,47]. Accordingly, 13t, at a concentration of 850 µM in 1.0 M HCl solution, achieved an IE% > 90%, showing that very low concentrations of 13t can provide adequate level of corrosion inhibition for MS in an acidic solution. In addition, its maximum inhibition efficiency is nearly equivalent to other azole derivatives reported in the literature [29–32]. The relevant impedance spectra and parameters for 1t, 1i, t, and i can be found in Fig. S4 and Table S2 in the Supplementary Information.

### 3.3. Weight loss measurements

Weight loss is a straightforward experiment that provides more physical and perceptible information for the evaluation of inhibitive performance. MS samples were immersed for  $12\,h$  in  $1.0\,M$  HCl solution to acquire information associated with long-term performance and effects of the inhibitors. The weight loss obtained for the MS substrates and the corresponding inhibition efficiency (IE $\%_{WI}$ ) is calculated as:

$$IE\%_{WL} = \frac{W_u - W_i}{W_u} \times 100\% \tag{7}$$

where  $W_u$  and  $W_i$  are the weight losses of MS in the uninhibited and inhibited solutions, respectively, and is summarized in Table 3. An inhibitor concentration of 850  $\mu$ M was used for all compounds.

Results showed that 13t had the lowest weight loss of 0.60  $\pm$  0.08 mg cm $^{-2}$ , which corresponded to a high IE% $_{WL}$  of  $\sim\!90.5\%$ . This inhibitor was then followed by 13i and 12i with IE% $_{WL}$  of  $\sim\!79.6\%$  and  $\sim\!74.6\%$ , respectively. A holistic analysis can be done by also including the IE% $_{WL}$  of 1t, 1i, t, and i. In their unmodified form, t and i had the lowest IE% $_{WL}$  and were ineffective due to their insufficient surface activity caused by their high solubility in water and low heteroatom reactivity [33,36]. On the other hand, 1t and 1i can better function as inhibitors due to the presence of an electron-donating phenyl group, which helps increase the electron density on the N heteroatoms and lower the solvation free energy [14,15]. This ability hinders the inhibitor dissociation and promotes

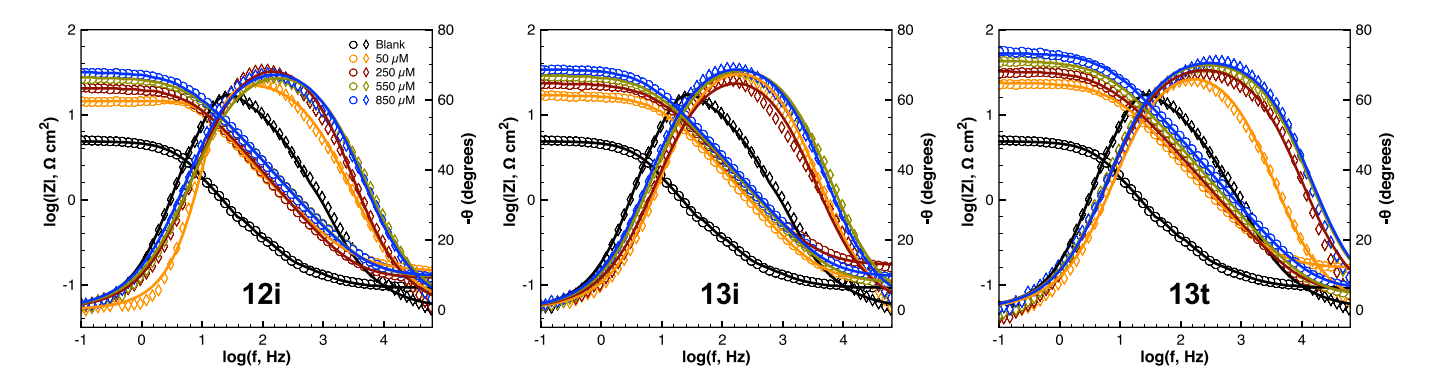


Fig. 4. Bode magnitude and phase angle plots, represented by open circles and diamonds, respectively, for MS in HCl solution in the absence and presence of 12i, 13i, and 13t at different concentrations. Fitted data are shown by solid lines.

Table 3 Weight loss data for MS after 12 h of immersion in 1.0 M HCl solution at 40  $^{\circ}\text{C}$  in the absence and presence of different azole inhibitors at 850  $\mu\text{M}$  in 1.0 M HCl solution.

	Weight loss (mg cm <sup>-2</sup> )	$IE_{WL}$ (%)
Blank	$6.32 \pm 0.26$	-
i	$4.69 \pm 0.17$	~25.7
t	$2.92 \pm 0.10$	~53.8
1i	$2.71 \pm 0.13$	~57.1
1 t	$1.91 \pm 0.25$	~69.8
12i	$1.61 \pm 0.16$	~74.6
13i	$1.29 \pm 0.12$	~79.6
13t	$0.60 \pm 0.08$	~90.5

enhanced adsorption on the metal surface. Furthermore, an additional Nheterocyclic ring on each 13t, 13i, and 12i inhibitor results in an improved shifting of electron density from the N atoms to the surface Fe atoms to achieve a stronger adsorption and better corrosion inhibition [33]. It has to be noted, however, that the inhibition efficiencies based on weight loss in Table 3 were not the same as those obtained from electrochemical experiments (Tables 1 and 2) as the former provides average corrosion rates, while the latter gives instantaneous rates [27]. 13t was an exception, however, as its IE%<sub>WL</sub> was relatively close to both IE<sub>o</sub> and IE%<sub>Z</sub>. This result, as supplemented by its Raman spectrum in Fig. 7a, showing evidence of an adsorptive inhibitor layer after the same immersion time, suggests that 13t can still be very efficient for up to 12 h. Nevertheless, the inhibition trend obtained from weight loss was in good agreement with the electrochemical results. To streamline our discussion, we considered 13t, 13i, and 12i, the top-performing inhibitors, to proceed with detailed investigation throughout our study.

#### 3.4. XRD

XRD was done to detect the presence of corrosion products on the metal surface. As shown in Fig. 5, all MS substrates produced three signature diffraction peaks for metallic Fe near  $45^{\circ}$ ,  $65^{\circ}$ , and  $82^{\circ}$ , which correspond to (110), (200), and (211) facets [52], respectively. While a small diffraction peak near  $35^{\circ}$  was seen for the uninhibited MS sample, corresponding to Fe oxidation and corrosion products [53] such as Fe<sub>2</sub>O<sub>3</sub>, FeOOH, and FeCl<sub>3</sub>, this same peak was also present in the 13i-inhibited MS but vanished in the presence of 13t. A higher peak intensity for Fe(110) near  $45^{\circ}$  was observed for 13t relative to the uninhibited and 13i-inhibited MS. This result

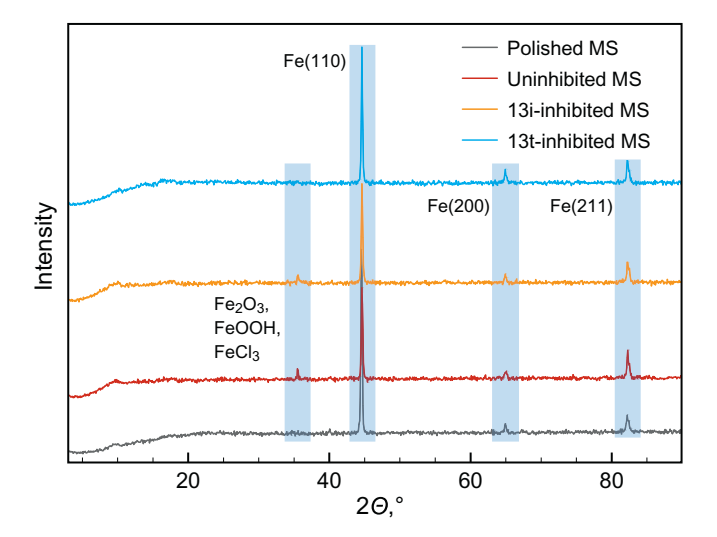


Fig. 5. XRD patterns for polished and 4-h-exposed MS samples to uninhibited and inhibited 1.0 M HCl solutions at 40  $^{\circ}$ C.

supports the formation of a protective film and a higher level of corrosion inhibition [54] in the presence of 13t.

#### 3.5. AFM study

AFM analysis was performed to investigate on a micro- and nanoscale the topographical feature and roughness of MS surfaces in the absence and presence of 850 µM inhibitor in HCl solution. Fig. 6 shows the three-dimensional images and root-mean-square roughness  $(R_q)$  values of MS surface in its polished form before and after a 4-h immersion. It is evident that the surface of the polished MS, prior to immersion, was moderately smooth with distinct abrading pattern and scratches, and a low  $R_a$  of ~24.1 nm. After exposure to the uninhibited acidic solution, the MS surface became extremely damaged with pits and deep holes and an increased  $R_a$  of ~196 nm was observed. With the presence of 13i, the surface topography showed improvement but with a slightly lower  $R_a$  of ~160 nm. This small drop in  $R_a$  is an indication of minor inhibition with some mild corrosion. This observation for 13i was in good agreement with its XRD pattern. However, in the presence of 13t, a significantly enhanced topography was achieved, giving an  $R_a$  value of ~43.2 nm, only twice that of the polished MS before immersion. Such improved surface smoothness can be attributed to the presence of a thin adsorptive layer of 13t, which retards corrosion by isolating the metal surface from the aggressive environment.

#### 3.6. SEM/EDX

In addition to AFM, the MS samples were also evaluated by SEM and EDX and the resulting morphologies and spectra before and after 4 h of exposure to uninhibited and inhibited HCl solutions are shown in Fig. 6 and S5, respectively. Prior to immersion, the morphology of MS showed a clean smooth surface and scratches due to polishing. The corresponding EDX spectrum showed signature elemental peaks associated with the composition of the metal. Pt peaks are due to the Pt coating applied to the MS surface prior to analysis to prevent electrical charging. The morphology of MS after immersion in the uninhibited solution showed cracks and pits, which are indications of a highly damaged surface due to acid corrosion attack. This damage is evidenced by the appearance of signal for O in the EDX spectrum, which confirms the formation of iron oxides. On the other hand, the morphology of the MS surfaces was improved by the addition of 13t and 13i such that the abrading scratches were still noticeable even after 4 h of immersion. The corresponding EDX spectra also displayed a decrease in O and Fe peaks, which implies that the inhibitors were able to decelerate corrosion. It is noteworthy that O peak was absent in the EDX spectrum for 13t-inhibited MS, which suggests that the inhibitor was effective in preventing electrochemical oxidation. Note that an N peak was not seen in the EDX spectra of the inhibited samples as the presence of C and its high mass absorption coefficient in its X-ray line induce a detection inefficiency for N [55]. As a result, many commonly designed EDX detectors produce very weak or no response for N and the detection can be often unreliable. Hence, the need for Raman spectroscopy to confirm the presence of an inhibitor film on the MS surface.

#### 3.7. Raman spectroscopy

The Raman spectra shown in Fig. 7a were recorded to confirm the interaction of 13t with the metal and its film formation on the surface. The Raman spectrum for  $13\ t$  in its powdered form showed the following bands [56]: in plane triazole trigonal breathing near  $1000\ cm^{-1}$ , N-N and C-N stretching at  $1146\ cm^{-1}$ , C-H in plane bonding near  $1285\ cm^{-1}$ , triazole ring stretching (N=N) modes between  $1375\ and\ 1425\ cm^{-1}$  and at  $1520\ cm^{-1}$ , and benzene ring stretching near  $1600\ cm^{-1}$ . In the spectrum for MS surface exposed to 13t-inhibited solution, the bands near  $1000\ cm^{-1}$  redshifted to  $975\ cm^{-1}$  and became a single broad band, while the small peak at  $1146\ cm^{-1}$  disappeared. These changes may be

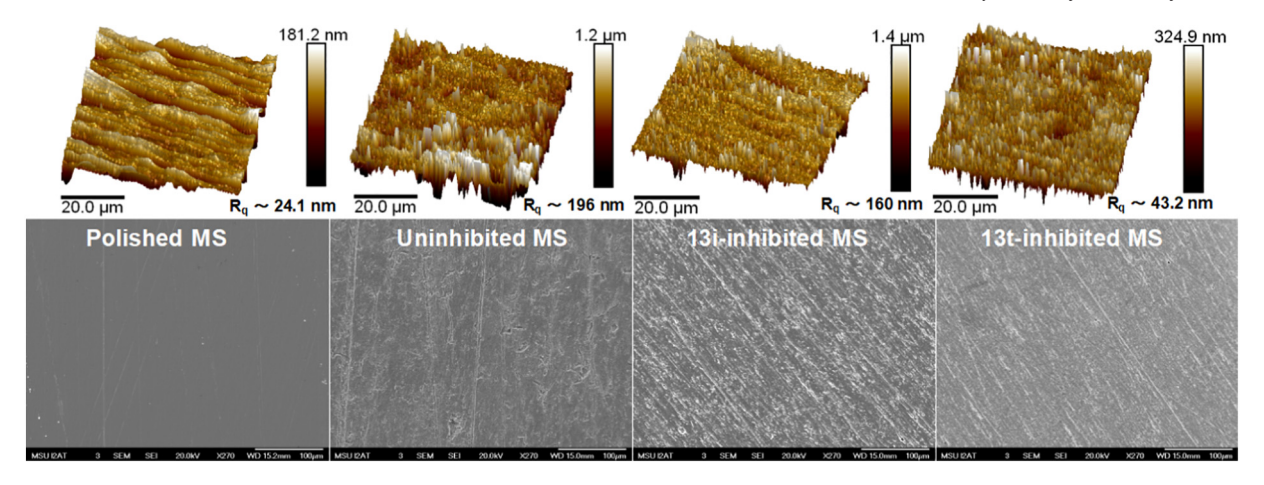


Fig. 6. Three-dimensional AFM (with  $R_q$  values) and SEM images for polished and 4-h-exposed MS samples to uninhibited and inhibited 1.0 M HCl solutions at 40 °C.

attributed to the Fe-N coordination during the interaction of 13t with the Fe surface via adsorption [57,58]. The decrease in peak intensity between 1375 and 1425 cm $^{-1}$  and at 1520 cm $^{-1}$  indicates that the triazoles may be very close to the MS surface and may have coordinated with Fe through the two sp $^2$  N atoms to form a compact protective film [57,58]

#### 3.8. Adsorption study

The efficiency of the inhibitors primarily depends on their ability to adsorb on the metal surface. It is, therefore, important to know the adsorption mode and isotherm, which can provide insights on the interaction of the azole-based molecules with the MS surface. Different isotherm models were tested and the best straight line fit was obtained by Langmuir isotherm [59], which shows the correlation between the inhibitor concentration  $C_i$  and surface coverage  $\Theta$  by the following equation:

$$\frac{C_i}{\Theta} = \frac{1}{K_{ads}} + C_i \tag{8}$$

where  $K_{ads}$  refers to the equilibrium adsorption constant, while  $\Theta$  is calculated using the  $R_p$  values obtained from EIS:

$$\Theta = \frac{R_{p,i} - R_{p,u}}{R_{p,i}} \tag{9}$$

From Fig. 7b, straight line fits were obtained for **13t**, **13i**, and **12i** for the plot  $C_i/\Theta$  versus  $C_i$ . The values for  $K_{ads}$  can be determined from the  $C_i/\Theta$ 

intercept.  $K_{ads}$  can also be correlated to  $\Delta G^{\circ}_{ads}$ , which refers to the standard Gibbs free energy of adsorption [60]:

$$\Delta G_{ads}^{\circ} = -RT \ln(55.55 K_{ads}) \tag{10}$$

where *R* and *T* refer to the gas constant and absolute temperature, respectively, while the value 55.55 is the molar concentration of water in the solution. The values for the adsorption parameters are summarized in Table 4.

The strong correlation, in which  $R^2 > 0.99$ , confirms that the inhibitor adsorption on the MS surface obeyed the Langmuir isotherm. This isotherm, which has been widely used in many corrosion inhibition studies [18,27,30,32,34], assumes that each inhibitor molecule occupies only one adsorption site and the adsorbed species do not interact with each other [59]. A slight slope increase from unity also confirms the interaction between the inhibitor molecules and Fe [18,30,32]. Higher  $K_{ads}$  value for 13t corresponds to enhanced adsorption and better inhibitive effect [34] than **13i** and **12i**, which had lower  $K_{ads}$  values.  $\Delta G_{ads}$ , which is a thermodynamic representation of  $K_{ads}$ , indicates the stability of inhibitor film formed on MS surface. The negative  $\Delta G_{ads}$  values imply that the adsorbed inhibitor layer exists at a lower free energy or more stable form compared to its preadsorption form [32,34]. In general,  $\Delta G_{ads}^{\circ}$  – 20 kJ mol<sup>-1</sup> describes physisorption, while  $\Delta G_{ads}^{\circ} \leq -40$  kJ mol<sup>-1</sup> depicts chemisorption. Since the calculated  $\Delta G_{ads}$  values ranged from -37 to -39 kJ mol<sup>-1</sup>, slightly less negative than  $-40 \text{ kJ} \text{ mol}^{-1}$ , the adsorption of the azolebased inhibitors is ascribed as primarily chemisorption with a minor amount of physisorption [32]. Upon exposure to HCl solution, MS is

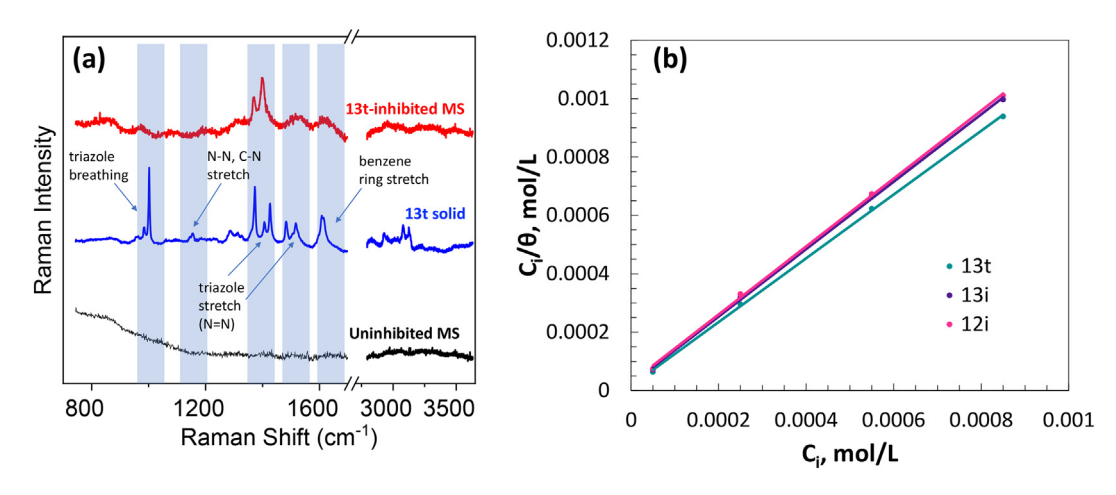


Fig. 7. (a) Raman spectra for 13t solid and MS samples after 12 h of immersion in uninhibited and 13t-inhibited 1.0 M HCl solutions at 40 °C. (b) Langmuir isotherm plots for the adsorption of 13t, 13i, and 12i on MS surface.

 $\begin{tabular}{ll} Table 4 \\ Adsorption parameters in the presence of $13$, $13$i, and $12$i on MS surface. \end{tabular}$ 

	13t	13i	12i
$K_{ads}$ (M <sup>-1</sup> )	61,850	44,640	36,180
$R^2$	0.9996	0.9995	0.9993
Slope	1.09	1.15	1.16
$\Delta G_{ads}^{\circ}(\text{kJ mol}^{-1})$	-39.16	-38.31	-37.77

oxidized to give a positively charged surface, on which Cl<sup>-</sup> ions from HCl can pre-adsorb. The azole-based inhibitors are protonated in acid solution and subsequently experience electrostatic attraction with the preadsorbed Cl<sup>-</sup> ions (physical adsorption). This phenomenon brings the inhibitor molecules closer to the MS surface where charge transfer can begin. The protonated inhibitor molecules may return to their neutral form by electron-transfer at the metal surface, forming a coordinate bond and releasing hydrogen gas. Since the formation constant between the metal ion and neutral inhibitor molecules is much larger than that of the protonated inhibitors, it is likely that Cl<sup>-</sup> ions on the MS surface are gradually replaced by neutral inhibitor molecules [30,32,35]. During this process, the electron lone pairs of N and the  $\pi$  electrons of -C=N and benzene ring promote chemical adsorption by transferring electrons to the unoccupied d-orbitals of Fe [27,28,33]. To relieve the buildup of negative charge on Fe, a retro-donation may occur, where electrons from the *d*-orbitals of Fe transfer back to the antibonding orbitals of the inhibitor molecules [27,28,32]. This activity further strengthens the inhibitor adsorption onto the metal surface. Thus, the entire inhibitor adsorption process may be viewed as a two-way mechanism initiated by physisorption and followed by chemisorption.

The Helmholtz model [61], can be used to describe the relationship between  $C_{db}$  electrode surface area (S), and film thickness (d):

$$C_{\rm dl} = \frac{\varepsilon \,^{\circ} eS}{d} \tag{11}$$

where  $\varepsilon^{\circ}$  and  $\varepsilon$  refer to the permittivity of air and local dielectric constant, respectively. The presence of an adsorptive inhibitor layer decreases the  $C_{dl}$  and electroactive area of MS surface exposed to acidic solution. This observation can be corroborated by determining the relative electroactive area (REA):

$$REA = 1 - \Theta \tag{12}$$

and plotting the resulting values against  $C_{dl}$ , where a linear correlation between the two parameters can be observed for 12i, 13i, and 13t (Fig. S6a). This relationship shows that  $\varepsilon/d$  is constant, suggesting the adsorption of inhibitor monolayer, and the  $C_{dl}$  values are related to the uninhibited (or electroactive) areas of MS surface [26]. In addition, linear extrapolation in Fig. S6a shows that  $C_{dl}$  approaches that of the blank solution when REA  $\approx 1$  (i.e. absence of corrosion inhibitor). The same correlation also exists between  $R_p$  and REA in Fig. S6b, where the decrease in electroactive area is associated with inhibitor film formation, which reduces intrusion of aggressive species into the MS surface. Similarly, as REA approaches 1 in Fig. S6b,  $R_p$  approaches the value experimentally determined in the blank solution, which, in principle, is purely  $R_{cb}$  owing to the absence of adsorbed inhibitor film on MS surface (i.e.  $R_f = 0$ ). Furthermore, when the  $R_p$  values are normalized by the REA, linear extrapolation of the plots in **Fig. S6c** intercepts the ordinates at values close to the  $R_p$  of the uninhibited system. This result indicates that the inhibitors block the active sites by forming an adsorptive layer on the MS surface [26].

# 3.9. DFT computations

DFT computations were performed to study the electronic and structural properties of the inhibitors and establish their correlation with inhibition efficiencies. The optimized structures for neutral and di-protonated 13t, 13i, and 12i, alongside their HOMO and LUMO are displayed in

Fig. 8. The optimized geometry for both neutral and protonated 13t revealed a more planar orientation compared to those for 13i and 12i. This planarity results in a higher surface coverage for 13t and enhanced adsorption efficiency. The same geometrical feature can be used to explain the improved corrosion inhibition of 13i over 12i, in which the imidazoles are at the meta position in the former, while at the ortho position in the latter. The LUMO and HOMO density distribution are also useful in identifying the reactive sites responsible for inhibitor adsorption on the metal surface [14,32]. For instance, the HOMO distribution for neutral 13i and 12i indicates that the imidazole rings are more accountable for donating electrons to Fe atoms, while their LUMO shows greater tendency for the benzene ring to accept electrons. For both the LUMO and HOMO of neutral 13t, however, the electron density is almost evenly distributed throughout the molecular surface. This uniformity provides greater directionality and flexibility for 13t to accept and donate electrons during its interaction with the metal surface.

To gain better insight into the adsorption and inhibition mechanism, the energy values and other intrinsic quantum chemical parameters of the azole-based inhibitors were obtained by DFT computations and the results are tabulated in Table 5. For both neutral and protonated forms, the trend for  $E_{LUMO}$  followed the sequence of  ${\bf 13t} < {\bf 13i}$ , suggesting that the efficiency of  ${\bf 13t}$  can be explained by its better potential to accept electrons from Fe atoms during retro-donation. The  $E_{HOMO}$  values, on the other hand, show that  ${\bf 13i}$  and  ${\bf 12i}$  are more disposed to donate electrons to Fe atoms compared to  ${\bf 13t}$ . However, the trend for  $E_{HOMO}$  did not follow the observed order for IE% obtained from electrochemical measurements, implying no correlation between  $E_{HOMO}$  and inhibitive strengths. It is noteworthy that the more negative  $E_{HOMO}$  and  $E_{LUMO}$  values for protonated inhibitors suggest less electron-donating capability and higher electron-accepting performance [14], respectively, than the neutral forms.

The energy gap ( $\Delta E$ ) is an essential parameter that describes the reactivity and adsorptivity of the inhibitor molecules:

$$\Delta E = E_{LUMO} - E_{HOMO} \tag{13}$$

The energy separation between LUMO and HOMO is an important factor in determining the degree of interaction between frontier molecular orbitals (FMO), that is, a smaller gap ( $\Delta E$ ) between  $E_{LUMO}$  and  $E_{HOMO}$ , increases the likelihood of a molecule to simultaneously donate and accept electrons [14]. Table 5 shows a slight difference in  $\Delta E$  between neutral 13t, 13i, and 12i, indicating similar donating and accepting electron ability. The protonated forms, however, revealed that the  $\Delta E$  of 13t was more than 1 eV lower than those for 13i and 12i, suggesting better inhibition, as also shown by the electrochemical and weight loss measurements, due to its versatility to perform electron transfer in both ways (i.e. from inhibitor to Fe and vice versa). This result also suggests that 13t has higher reactivity and better adsorptivity in its protonated form than in its neutral form.

Other quantum chemical parameters such as electronegativity (*EN*) and global hardness ( $\eta$ ) are also calculated as follows [62]:

$$EN = -0.5(E_{HOMO} + E_{LUMO}) \tag{14}$$

$$\eta = -0.5(E_{HOMO} - E_{LUMO}) \tag{15}$$

The higher *EN* observed for neutral and protonated **13t** corresponds to a higher electron-attracting ability compared to **13i** and **12i**. It can also be seen that *EN* is enhanced after protonation, suggesting that the protonated inhibitors attract electrons more easily than their neutral forms. This *EN* increase means that the protonated inhibitors play an essential role in coordinating with the metal during retro-donation.

Chemical hardness is an important property that describes the inhibitor's degree of adsorption on the metal surface [14,30,31,62]. In general, an organic inhibitor can be regarded as a soft base, while a metal as a soft acid [63]. Therefore, inhibitor adsorption on a metal surface can be thought of as a soft-soft interaction and inhibitors with higher softness feature (lower  $\eta$ ) contribute more favorably to such interaction [14]. From

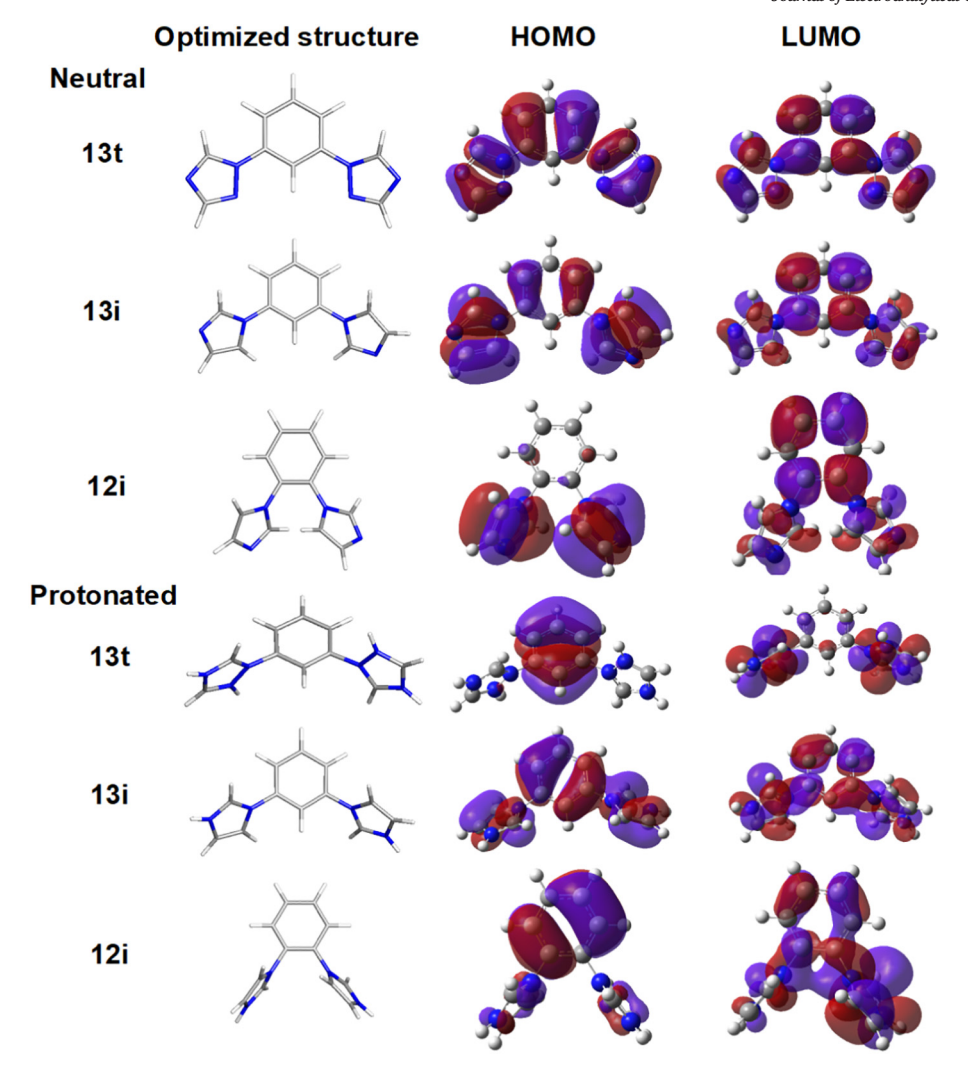


Fig. 8. Optimized structures and FMOs of neutral and di-protonated 13t, 13i, and 12i. Color code: blue, N; red, O; gray, C; white, H.

Table 5, protonated **13t** showed the smallest  $\eta$  value corresponding to a maximum softness characteristic, which also means that **13t**, in its protonated form, strongly adsorbs on the MS surface to achieve the maximum inhibition efficiency as shown by the IE%<sub>o</sub> and IE%<sub>z</sub>.

Furthermore, the fraction of electrons transferred ( $\Delta N$ ) is another important parameter that can be estimated by the Pearson electronegativity scale [64]:

$$\Delta N = \frac{\phi - EN_i}{2(\eta_{Fe} + \eta_i)} \tag{16}$$

**Table 5**Quantum chemical parameters obtained from DFT calculations for the azole-based inhibitors in their neutral and protonated forms.

	Neutral			Protonated	nted		
	13t	13i	12i	13t	13i	12i	
$E_{HOMO}$	-6.727	-6.326	-6.182	-21.384	-14.075	-14.235	
$E_{LUMO}$	-1.422	-1.106	-1.096	-16.680	-8.076	-8.305	
$\Delta E$	5.305	5.220	5.086	4.704	5.999	5.930	
EN	4.075	3.716	3.639	19.032	11.076	11.270	
η	2.653	2.610	2.543	2.352	3.000	2.965	
$\Delta N$	0.141	0.211	0.232	-3.021	-1.043	-1.088	

Note: All values are in eV.

where  $\phi$  is the work function of Fe surface with a value of 4.82 eV for Fe (110) [64],  $EN_i$  is the electronegativity of the inhibitor (from Eq. (14)), while  $\eta_i$  and  $\eta_{Fe}=0$  [62] are the global hardness of the inhibitor (from Eq. (15)) and Fe, respectively.  $\Delta N$  indicates whether electrons are transferred from the inhibitor molecule to the metal ( $\Delta N>0$ ) or vice versa ( $\Delta N<0$ ) [15]. The positive  $\Delta N$  values from Table 5 confirms the transfer of electrons from inhibitors in their neutral form to Fe during chemisorption. On the other hand, the negative  $\Delta N$  values explain that during retrodonation, electrons are mostly transferred to the protonated inhibitors, with more electron transfer propensity towards 13t due to its more negative  $\Delta N$  value compared to 13i and 12i. Combined with the results from other chemical quantum parameters, it is thought that the stronger capacity for 13t to accept electrons accounted for its higher IE% compared to 13i and 12i.

#### 4. Conclusions

The azole-based compounds namely, **13t**, **13i**, and **12i** have proven to be useful and effective as corrosion inhibiting agents for MS in acidic medium. Their inhibitive properties stem primarily from their molecular structure, which features an aromatic ring with N-heterocyclic azole substituents capable of adsorbing on a metal surface to form a protective layer that can block active corrosion sites. This adsorption, evidenced

by Raman spectroscopy, is mainly facilitated by an electron transfer process between the inhibitor molecule and metallic Fe surface that results in an adsorbed Fe-inhibitor complex. Electrochemical measurements revealed that low concentrations of 13t in HCl solution at  $40\,^{\circ}\text{C}$  exhibited the highest inhibition efficiency owing to its structural planarity and the presence of more N heteroatoms. As a result, more effective adsorption was achieved compared to 13i and 12i. Also, the ability of 13t is mostly credited to its greater capacity to accept electrons, in contrast to both 13i and 12i due to a higher inclination to donate electrons. Overall, these azole-based compounds may be used as inexpensive, less complicated, and environmentally friendly corrosion inhibitors at the  $\mu\text{M}$  level in acid pickling and other industrial applications that involve harsh and elevated temperature conditions.

#### **Declaration of Competing Interest**

The authors declare that they have no known competing financial interests or personal relationships that could have appeared to influence the work reported in this paper.

#### Acknowledgements

This work has been supported by the Department of Chemistry and Marvin B. Dow Advanced Composites Institute at Mississippi State University. Computations were performed at the Mississippi Center for Supercomputing Research (MCSR). This study was also partly supported by the Mississippi State University Office of Research and Economic Development and the National Science Foundation (OIA-1539035).

#### Appendix A. Supplementary data

Supplementary data to this article can be found online at https://doi.org/10.1016/j.jelechem.2020.114858.

#### References

- [1] N.K. Singh, E. Cadoni, M.K. Singha, N.K. Gupta, Dynamic tensile and compressive behaviors of mild steel at wide range of strain rates, J. Eng. Mech. 139 (2013) 1197–1206.
- [2] J.X. Fu, L. Chen, C.J. Wu, Y.X. Wu, Marine engineering steels-properties requirements and evaluation, Trans Tech Publ 2014, pp. 465–469.
- [3] E.A. Noor, A.H. Al-Moubaraki, Corrosion behavior of mild steel in hydrochloric acid solutions, Int. J. Electrochem. Sci. 3 (2008) 806–818.
- [4] N.F. Atta, A. Fekry, H.M. Hassaneen, Corrosion inhibition, hydrogen evolution and antibacterial properties of newly synthesized organic inhibitors on 316L stainless steel alloy in acid medium, Int. J. Hydrog. Energy 36 (2011) 6462–6471.
- [5] E.B. Caldona, D.W. Smith, D.O. Wipf, Protective action of semi-fluorinated perfluorocyclobutyl polymer coatings against corrosion of mild steel, J. Mater. Sci. 55 (2020) 1796–1812.
- [6] E.B. Caldona, A.C.C. De Leon, P.G. Thomas, D.F. Naylor III, B.B. Pajarito, R.C. Advincula, Superhydrophobic rubber-modified polybenzoxazine/SiO2 nanocomposite coating with anticorrosion, anti-ice, and superoleophilicity properties, Ind. Eng. Chem. Res. 56 (2017) 1485–1497.
- [7] E.B. Caldona, C. Al Christopher, J.D. Mangadlao, K.J.A. Lim, B.B. Pajarito, R.C. Advincula, On the enhanced corrosion resistance of elastomer-modified polybenzoxazine/graphene oxide nanocomposite coatings, React. Funct. Polym. 123 (2018) 10–19.
- [8] E.B. Caldona, C. Al Christopher, B.B. Pajarito, R.C. Advincula, Novel anti-corrosion coatings from rubber-modified polybenzoxazine-based polyaniline composites, Appl. Surf. Sci. 422 (2017) 162–171.
- [9] M. Goyal, S. Kumar, I. Bahadur, C. Verma, E.E. Ebenso, Organic corrosion inhibitors for industrial cleaning of ferrous and non-ferrous metals in acidic solutions: a review, J. Mol. Liq. 256 (2018) 565–573.
- [10] G. Gece, Drugs: a review of promising novel corrosion inhibitors, Corros. Sci. 53 (2011) 3873–3898.
- [11] P.B. Raja, M.G. Sethuraman, Natural products as corrosion inhibitor for metals in corrosive media—a review, Mater. Lett. 62 (2008) 113–116.
- [12] C.V. King, E. Goldschmidt, N. Mayer, Inorganic corrosion inhibitors in acid solution, J. Electrochem. Soc. 99 (1952) 423–426.
- [13] S.E. Manahan, Fundamentals of Environmental Chemistry, third ed. CRC Press, 2011.
- [14] N. Khalil, Quantum chemical approach of corrosion inhibition, Electrochim. Acta 48 (2003) 2635–2640.

- [15] I. Lukovits, E. Kalman, F. Zucchi, Corrosion inhibitors—correlation between electronic structure and efficiency, Corrosion. 57 (2001) 3–8.
- [16] W. Frenier, F. Growcock, V. Lopp, α-Alkenylphenones—a new class of acid corrosion inhibitors, Corrosion 44 (1988) 590–598.
- [17] K. Neemla, R. Saxena, A. Jayaraman, Corrosion inhibition of oil-well equipment during acidization, Corros. Prev. Control. 39 (1992) 69–73.
- [18] H. Lgaz, R. Salghi, S. Jodeh, B. Hammouti, Effect of clozapine on inhibition of mild steel corrosion in 1.0 M HCl medium, J. Mol. Liq. 225 (2017) 271–280.
- [19] P.B. Matad, P.B. Mokshanatha, N. Hebbar, V.T. Venkatesha, H.C. Tandon, Ketosulfone drug as a green corrosion inhibitor for mild steel in acidic medium, Ind. Eng. Chem. Res. 53 (2014) 8436–8444.
- [20] S.K. Shukla, M. Quraishi, Cefalexin drug: a new and efficient corrosion inhibitor for mild steel in hydrochloric acid solution, Mater. Chem. Phys. 120 (2010) 142–147.
- [21] S.K. Shukla, A.K. Singh, I. Ahamad, M. Quraishi, Streptomycin: a commercially available drug as corrosion inhibitor for mild steel in hydrochloric acid solution, Mater. Lett. 63 (2009) 819–822.
- [22] A. Fouda, G. El-Ewady, A. Ali, Modazar as promising corrosion inhibitor of carbon steel in hydrochloric acid solution, Green Chem. Lett. Rev. 10 (2017) 88–100.
- [23] Y. Qiang, S. Zhang, B. Tan, S. Chen, Evaluation of Ginkgo leaf extract as an eco-friendly corrosion inhibitor of X70 steel in HCl solution. Corros. Sci. 133 (2018) 6–16.
- [24] M. Prabakaran, S.-H. Kim, K. Kalaiselvi, V. Hemapriya, I.-M. Chung, Highly efficient Ligularia fischeri green extract for the protection against corrosion of mild steel in acidic medium: electrochemical and spectroscopic investigations, J. Taiwan Inst. Chem. Eng. 59 (2016) 553–562.
- [25] M. Prabakaran, S.-H. Kim, V. Hemapriya, I.-M. Chung, Tragia plukenetii extract as an eco-friendly inhibitor for mild steel corrosion in HCl 1 M acidic medium, Res. Chem. Intermed. 42 (2016) 3703–3719.
- [26] C.M. Fernandes, T.S.F. da Fagundes, N.E. dos Santos, T.S.M. de Rocha, R. Garrett, R.M. Borges, G. Muricy, A.L. Valverde, E.A. Ponzio, *Ircinia strobilina* crude extract as corrosion inhibitor for mild steel in acid medium, Electrochim. Acta 312 (2019) 137–148.
- [27] W. Li, Q. He, S. Zhang, C. Pei, B. Hou, Some new triazole derivatives as inhibitors for mild steel corrosion in acidic medium, J. Appl. Electrochem. 38 (2008) 289–295.
- [28] F. Bentiss, M. Lagrenee, M. Traisnel, J. Hornez, The corrosion inhibition of mild steel in acidic media by a new triazole derivative, Corros. Sci. 41 (1999) 789–803.
- [29] H. Ouici, M. Tourabi, O. Benali, C. Selles, C. Jama, A. Zarrouk, F. Bentiss, Adsorption and corrosion inhibition properties of 5-amino 1, 3, 4-thiadiazole-2-thiol on the mild steel in hydrochloric acid medium: thermodynamic, surface and electrochemical studies, J. Electroanal. Chem. 803 (2017) 125–134.
- [30] A. Dutta, S.K. Saha, U. Adhikari, P. Banerjee, D. Sukul, Effect of substitution on corrosion inhibition properties of 2-(substituted phenyl) benzimidazole derivatives on mild steel in 1 M HCl solution: a combined experimental and theoretical approach, Corros. Sci. 123 (2017) 256–266.
- [31] J. Haque, V. Srivastava, C. Verma, M. Quraishi, Experimental and quantum chemical analysis of 2-amino-3-((4-(S)-2-amino-2-carboxyethyl)-1H-imidazol-2-yl) thio) propionic acid as new and green corrosion inhibitor for mild steel in 1 M hydrochloric acid solution, J. Mol. Liq. 225 (2017) 848–855.
- [32] K. Ansari, M. Quraishi, A. Singh, Schiff's base of pyridyl substituted triazoles as new and effective corrosion inhibitors for mild steel in hydrochloric acid solution, Corros. Sci. 79 (2014) 5–15.
- [33] Y.I. Kuznetsov, L. Kazansky, Physicochemical aspects of metal protection by azoles as corrosion inhibitors, Russ. Chem. Rev. 77 (2008) 219.
- [34] J. Aljourani, K. Raeissi, M. Golozar, Benzimidazole and its derivatives as corrosion inhibitors for mild steel in 1M HCl solution, Corros. Sci. 51 (2009) 1836–1843.
- [35] M. Faisal, A. Saeed, D. Shahzad, N. Abbas, F.A. Larik, P.A. Channar, T.A. Fattah, D.M. Khan, S.A. Shehzadi, General properties and comparison of the corrosion inhibition efficiencies of the triazole derivatives for mild steel, Corros. Rev. 36 (2018) 507–545.
- [36] K. Khaled, Molecular simulation, quantum chemical calculations and electrochemical studies for inhibition of mild steel by triazoles, Electrochim. Acta 53 (2008) 3484–3492.
- [37] W.D. Clark, G.E. Tyson, T.K. Hollis, H.U. Valle, E.J. Valente, A.G. Oliver, M.P. Dukes, Toward molecular rotors: tetra-N-heterocyclic carbene Ag (I)-halide cubane-type clusters, Dalton Trans. 42 (2013) 7338–7344.
- [38] S.-B. Ko, H.-J. Park, S. Gong, X. Wang, Z.-H. Lu, S. Wang, Blue phosphorescent N-heterocyclic carbene chelated Pt (II) complexes with an α-duryl-β-diketonato ancillary ligand, Dalton Trans. 44 (2015) 8433–8443.
- [39] Y.H. So, Novel thermoset polyimidazole amides, Macromolecules. 25 (1992) 516–520.
- [40] M. Frisch, G. Trucks, H. Schlegel, G. Scuseria, M. Robb, J. Cheeseman, G. Scalmani, V. Barone, G. Petersson, H. Nakatsuji, X. Li, M. Caricato, A.V. Marenich, J. Bloino, B.G. Janesko, R. Gomperts, B. Mennucci, H.P. Hratchian, J.V. Ortiz, A.F. Izmaylov, J.L. Sonnenberg, F. Ding Williams, F. Lipparini, F. Egidi, J. Goings, B. Peng, A. Petrone, T. Henderson, D. Ranasinghe, V.G. Zakrzewski, J. Gao, N. Rega, G. Zheng, W. Liang, M. Hada, M. Ehara, K. Toyota, R. Fukuda, J. Hasegawa, M. Ishida, T. Nakajima, Y. Honda, O. Kitao, H. Nakai, T. Vreven, K. Throssell, J.A. Montgomery Jr., J.E. Peralta, F. Ogliaro, M.J. Bearpark, J.J. Heyd, E.N. Brothers, K.N. Kudin, V.N. Staroverov, T.A. Keith, R. Kobayashi, J. Normand, K. Raghavachari, A.P. Rendell, J.C. Burant, S.S. Iyengar, J. Tomasi, M. Cossi, J.M. Millam, M. Klene, C. Adamo, R. Cammi, J.W. Ochterski, R.L. Martin, K. Morokuma, O. Farkas, J.B. Foresman, D.J. Fox, Gaussian 16, Revision A. 03, Gaussian, Inc., Wallingford, CT, Technical Report, 2016.
- [41] P.J. Stephens, F. Devlin, C. Chabalowski, M.J. Frisch, Ab initio calculation of vibrational absorption and circular dichroism spectra using density functional force fields, J. Phys. Chem. 98 (1994) 11623–11627.
- [42] A. Becke, Density-functional thermochemistry. III. The role of exact exchange, J. Chem. Phys. 98 (1993) 5648.

- [43] C. Lee, W. Yang, R.G. Parr, Development of the Colle-Salvetti correlation-energy formula into a functional of the electron density, Phys. Rev. B 37 (1988) 785.
- [44] B. Miehlich, A. Savin, H. Stoll, H. Preuss, Results obtained with the correlation energy density functionals of Becke and Lee, Yang and Parr, Chem. Phys. Lett. 157 (1989) 200–206.
- [45] W.J. Hehre, R. Ditchfield, J.A. Pople, Self—consistent molecular orbital methods. XII. Further extensions of Gaussian—type basis sets for use in molecular orbital studies of organic molecules, J. Chem. Phys. 56 (1972) 2257–2261.
- [46] P.C. Hariharan, J.A. Pople, The influence of polarization functions on molecular orbital hydrogenation energies, Theor. Chim. Acta 28 (1973) 213–222.
- [47] L. Antropov, E. Makushin, V. Panasenko, Metal corrosion inhibitors, Kiev. Tech. (1981) 182.
- [48] H.M. Abd El-Lateef, Experimental and computational investigation on the corrosion inhibition characteristics of mild steel by some novel synthesized imines in hydrochloric acid solutions, Corros. Sci. 92 (2015) 104–117.
- [49] J.R. Macdonald, E. Barsoukov, in: J.R. Macdonald, E. Barsoukov (Eds.), Impedance Spectroscopy: Theory, Experiment, and Applications, Wiley 2005, pp. 1–13.
- [50] C. Hsu, F. Mansfeld, Concerning the conversion of the constant phase element parameter Y0 into a capacitance, Corrosion. 57 (2001) 747–748.
- [51] Z. Stojek, The electrical double layer and its structure, in: F. Scholz (Ed.), Electroanalytical Methods, Springer-Verlag, Berlin Heildelberg 2010, pp. 3–9.
- [52] H.D. Omar, To investigation the structure and morphology of iron metallic by difference techniques, J. Nano. Adv. Mat. 3 (2015) 57–61.
- [53] Y. Takahashi, E. Matsubara, S. Suzuki, Y. Okamoto, T. Komatsu, H. Konishi, J. Mizuki, Y. Waseda, In-situ X-ray diffraction of corrosion products formed on iron surfaces, Mater. Trans. 46 (2005) 637–642.

- [54] P. Sakunthala, S.S. Vivekananthan, M. Gopiraman, N. Sulochana, A.R. Vincent, Spectroscopic investigations of physicochemical interactions on mild steel in an acidic medium by environmentally friendly green inhibitors, J. Surfactant Deterg. 16 (2013) 251–263.
- [55] Y. Liao, Practical electron microscopy and database, http://www.globalsino.com/EM/ (accessed May 30, 2020).
- [56] F. Adar, Introduction to interpretation of Raman spectra using database searching and functional group detection and identification, Spectroscopy. 31 (2016) 16–23.
- [57] D. Thierry, C. Leygraf, Enhanced Raman scattering of 1, 2, 4-triazole and imidazole adsorbed on microlithographically prepared copper surfaces, J. Electrochem. Soc. 133 (1986) 2236–2239.
- [58] P. Cao, R. Gu, Z. Tian, Electrochemical and surface-enhanced Raman spectroscopy studies on inhibition of iron corrosion by benzotriazole, Langmuir. 18 (2002) 7609–7615.
- [59] I. Langmuir, The evaporation, condensation and reflection of molecules and the mechanism of adsorption, Phys. Rev. 8 (1916) 149.
- [60] J.W. Gibbs, A method of geometrical representation of the thermodynamic properties by means of surfaces, Trans. Connecticut Acad. Arts Sci. (1873) 382-404.
- [61] H.V. Helmholtz, Studien Über Electrische Grenzschichten, Ann. Phys. 243 (1879) 337–382.
- [62] R.G. Parr, R.G. Pearson, Absolute hardness: companion parameter to absolute electronegativity, J. Am. Chem. Soc. 105 (1983) 7512–7516.
- [63] R.G. Pearson, Hard and soft acids and bases, J. Am. Chem. Soc. 85 (1963) 3533-3539.
- 64] R.G. Pearson, Absolute electronegativity and hardness: application to inorganic chemistry, Inorg. Chem. 27 (1988) 734–740.